Testing the Limitations of 2-D Companding for Strain Imaging Using Phantoms

Pawan Chaturvedi, *Member, IEEE*, Michael F. Insana, *Member, IEEE*, and Timothy J. Hall, *Member, IEEE*

***Abstract*—Companding may be used as a technique for generating low-noise strain images. It involves warping radio-frequency echo fields in two dimensions and at several spatial scales to minimize decorrelation errors in correlation-based displacement estimates. For the appropriate experimental conditions, companding increases the sensitivity and dynamic range of strain images without degrading contrast or spatial resolution significantly.**

In this paper, we examine the conditions that limit the effectiveness of 2-D local companding through a series of experiments using phantoms with tissue-like acoustic and elasticity properties. We found that strain noise remained relatively unchanged as the applied compression increased to 5% of the phantom height, while target contrast increased in proportion to the compression. Controlling the image noise at high compressions improves target visibility over the broad range induced in elastically heterogeneous media, such as biological tissues. Compressions greater than 5% introduce large strains and complex motions that reduce the effectiveness of companding. Control of boundary conditions and ultrasonic data sampling rates is critical for a successful implementation of our algorithms.

I. Introduction

The relative stiffness of soft biological tissues, as described by strain images, has the potential to be a sensitive indicator of some breast cancers [1], [2] and renal diseases [3]. Strain images are formed from measurements of local displacements induced by compressive forces applied to tissue surfaces. The displacement fields are estimated using correlation techniques that track echo delays in segmented waveforms recorded before and after static compression [4], [5].

It is well-known that the most precise displacement estimates, and consequently the lowest-noise strain images, are obtained when the compressive forces shift echoes along the time axis without decorrelating the signals, and the shifts are constant with time over the duration of the correlation windows, e.g., rigid-body motion [6]. When echo delays are constant and the time-bandwidth product of the echo waveforms is large, cross-correlation is an efficient delay estimator in the sense that strain estimates achieve the Crámer-Rao lower bound for variance [6], [7]. Strain estimates under these conditions are limited only by the operating frequency and the signal-to-noise ratio of the ultrasound signals.

When the precompression echo signal at an instant in time is highly correlated with the postcompression echo signal at another instant in time, but the delays vary over the duration of the data window, correlation-based time delay estimators suffer large errors because of time-averaged signal decorrelation. In this situation, the ability of a cross-correlator to track motion is reduced because correlation is lost between waveforms averaged over the data window. The challenge is to generate large strains in the tissue to maximize contrast for stiffness variations while simultaneously maintaining high echo-signal correlation for precise time delay estimation and minimal noise.

An effective way to restore correlation lost from either time-averaged signal decorrelation or nonaxial tissue motion is to compand (compress and/or expand) one of the two echo fields prior to cross-correlation. Previously we proposed a multi-scale, 2-D local compander for strain imaging [8]. It was based on the computationally efficient sum-absolute-difference (SAD) method for motion detection that involved a block-matching algorithm [9]–[11]. Successful 2-D companding requires that the object motion be confined to the ultrasonic scan plane. Displacements are then measured locally on a coarse grid to align pre- and postcompression echo fields on a scale greater than 1 mm. This reduces the deformations that cause large decorrelation errors when 1-D axial cross-correlators are applied to estimate fine-scale displacements ($<$1 mm). Signal conditioning by 1-D companding has been used for more than 20 years by the signal processing community as a means for minimizing time delay errors, e.g., [7], [12], [13].

Companding is most effective when there is minimal instantaneous signal decorrelation, i.e., under the ideal condition where the postcompression echo field can be expressed as a time-scaled and time-shifted copy of the precompression echo field [6]. A common source of instantaneous decorrelation is a redistribution of scatterers within the resolution cell volume caused by external compression [14]. Ideal conditions are achieved when the bandwidth of the acoustic pulse is larger than that of the tissue reflectivity spectrum, all tissue motion is confined to the scan plane, and the echo data are finely sampled. Under these conditions, movement of each scatterer can be tracked precisely in 2-D. Displacements found by companding are used to warp the precompression echo field to match the postcompression field. Only those displacements in the direc-

Manuscript received August 15, 1997; accepted February 9, 1998. This work was supported by NIH grant P01 CA64597 (through the University of Texas) and the Clinical Radiology Foundation at KUMC.

The authors are with the Department of Radiology, University of Kansas Medical Center, Kansas City, KS 66160–7234 (e-mail: pawan@research.kumc.edu).

tion of the ultrasound beam axis are stored. The residual axial displacement field is then estimated on a fine spatial scale using 1-D cross-correlation, the results are added to the axial component of displacements found during the local companding step, and the gradient of the sum along the beam axis is the strain image. This multi-scale approach to displacement estimation greatly reduces noise in the strain image without significantly reducing spatial resolution or contrast [8]. For the appropriate conditions, companded strain images have contrast-to-noise ratios far superior to that of noncompanded images.

In practice, however, the 2-D ultrasonic bandwidth is smaller than the bandwidth of the tissue response spectrum, and it can be difficult to restrict all motion to the scan plane in heterogeneous tissues even with surface restraints. Nevertheless, the companding assumptions are met in practice for large, single compression steps, as shown below, because the strain profile varies slowly throughout the tissue, even for large displacement.

Other researchers have used multicompression techniques to reduce strain noise for large compressions [3], [4], [15]. Displacements are accumulated over time from many small compressions to minimize strain in the correlation window. With multicompression methods, decorrelation errors from all sources are minimized; in particular, the effects of out-of-plane motion are negligible. However, the contrast in a strain image is proportional to the amount of compression applied during each increment. Therefore, noise is reduced at the expense of contrast. Also, multicompression methods require large data volumes and long computation times as compared with companding methods. If the ultrasonic signal-to-noise ratio is low, multicompression strain images become noisy, and registration problems can reduce spatial resolution. It is likely that both approaches have a future in strain imaging, where together they increase the dynamic range for strain significantly and efficiently.

The focus of this paper is the use of tissue-mimicking phantoms to explore the limitations of companding under imaging situations similar to those expected to be encountered in clinical applications. Specifically, we aimed to find how much compression can be applied under various boundary conditions before the companding assumptions break down, and the increase in instantaneous decorrelation noise surpasses the increase in strain contrast provided by large compressions; in those situations, multicompression has an advantage over companding. We also investigated whether the orientation of applied compression with respect to the sound beam had any effect on strain images obtained with 2-D companding.

II. Methods

A. The Phantom

The graphite-gelatin phantom illustrated in Fig. 1(a) was used to investigate the limitations of 2-D companding for improved target visibility in strain images. The phantom was rectangular, 10 cm × 10 cm × 7.4 cm (height), and contained three cylindrical inclusions extending the full depth and positioned along a diagonal. The background material was elastically homogeneous with a Young's modulus of 25 kPa. The axes of the cylindrical inclusions were parallel to each other and perpendicular to the image plane as shown. The inclusions, each 8.7 mm in diameter, were approximately three times stiffer than the background (80 kPa). The elastic properties of the phantom were designed to mimic the relative stiffness of breast tumors in situ[1]. Materials construction and elastic modulus measurements are described in [16]. The entire top surface of the phantom was compressed from above while the bottom surface was fixed along the z axis only. Each contact surface of the phantom was lubricated to allow free slippage except where noted in Section III. The phantom was precompressed 4% of its height to establish acoustic contact with the transducer, unless otherwise stated. Fig. 1(c) shows the predicted 2-D strain profile of the phantom experiment as obtained through finite-element analysis assuming linear, elastic media under the experimental conditions described below.

B. The Measurement

A linear array (5L45, Quantum 2000, Siemens Ultrasound, Inc., Issaquah, WA) was flush mounted to the compressor surface. The planar compressor was mounted in the x, y plane and attached to a linear table that was moved along the z axis by a computer-controlled stepper motor whose position was monitored by an optical encoder. The position was accurately controlled within 0.04 mm. The 5 MHz, f/2 array with 60% bandwidth, 45 mm elevational focal length, and 5 mm^{-1} echo line density, was used to record the 200 rf waveforms of the echo field, each 60 μs in duration, at a sampling rate of 50 Msamples/s. The 20 dB lateral and elevational half beam widths over the image were approximately 0.6 mm and 0.9 mm, respectively. A LeCroy TR8828C system (LeCroy, Inc., New York) was used to acquire the data. The echo field, 40 mm × 46.2 mm in dimensions, was located in the middle of the phantom as indicated by the solid white line in Fig. 1(a). The recording system is detailed in Fig. 1 of [17]. Signal processing and image formation were conducted off-line on a DEC alpha workstation in 10 to 30 minutes per strain image.

C. Image Formation

The imaging procedure begins with three-step displacement estimation, as outlined in Fig. 2. First, the precompression echo field is shifted and companded as a unit in two dimensions. In Step 1 the echo field is globally deformed in 2-D according to the average applied tissue deformation. Second, 2-D local companding is applied to locally deform the precompression echo field. Step 2 warps

[1]Unpublished data from T. A. Krouskop, Baylor College of Medicine, Houston, TX.

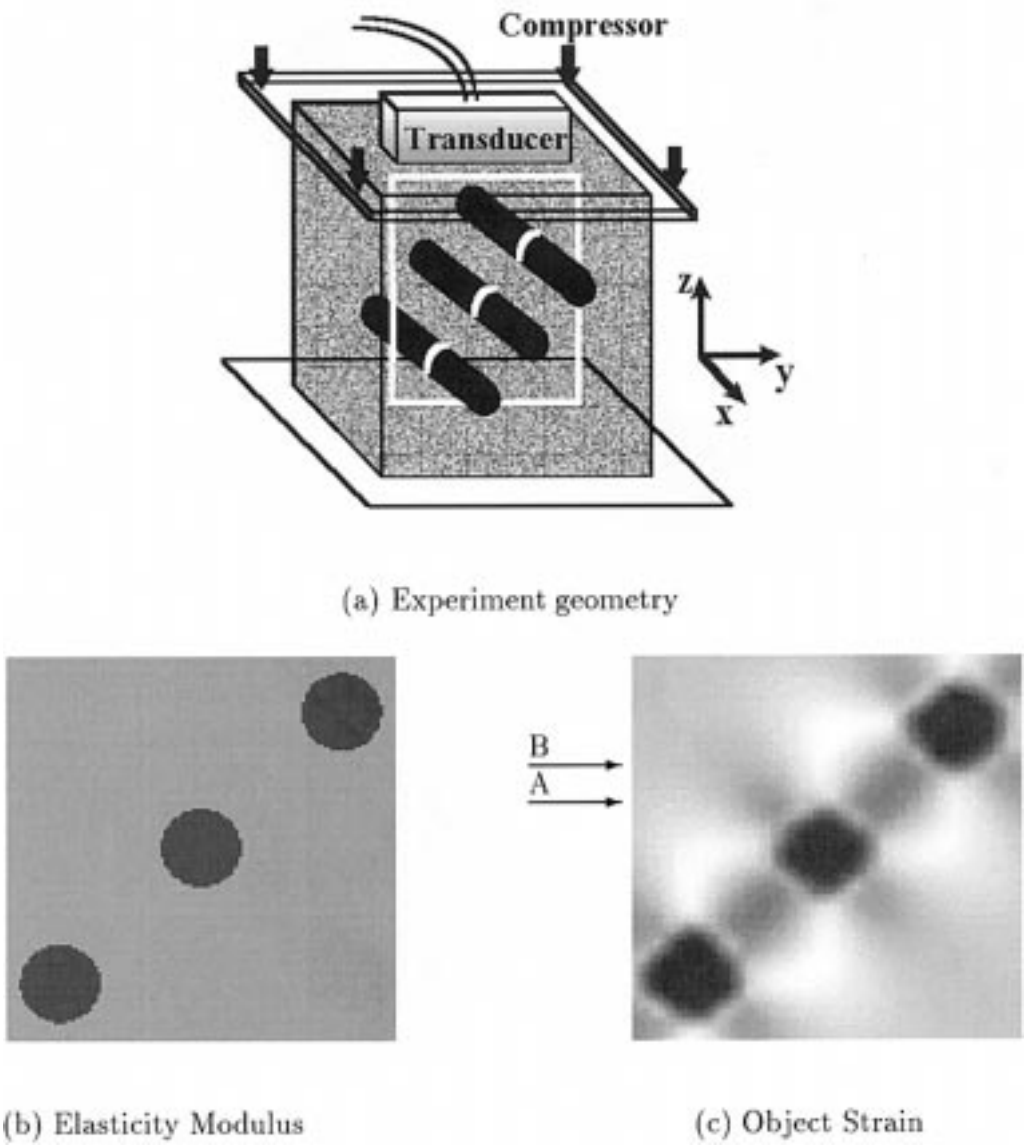

Fig. 1. (a) Diagram of the gelatin phantom, scanning apparatus, and coordinate system. (b) The elastic modulus profile in the y, z scan plane. The Young's modulus was 80 kPa in the dark inclusions and 25 kPa in the background. (c) The strain profile is shown for constant displacement of the top surface along $-z$ for free slip of the top and bottom surfaces in the x, y plane. The strain profile is modeled using a linear-stress finite-element algorithm (Algor, Inc., Pittsburgh, PA).

the precompression echo field according to a low-resolution estimate of displacement. If the sample is elastically homogeneous, local companding will detect no motion for the uniform stress applied. The SAD algorithm of [11] was adapted for steps 1 and 2 as described by [8]. It is used to estimate displacement by finding the minimum sum-absolute difference between rf echo data in a pre- and post-compression data kernel. Users supply the kernel size and 2-D search region over which the SAD value is computed. Step 2 is sufficient to restore correlation; however, processing time is greatly reduced when step 2 is used in conjunction with step 1. Third, any residual axial displacement is estimated by cross-correlation methods [4]–[6], [13]. The axial displacement field used for strain estimation is the sum of steps 2 and 3 because step 1 provides no information about local strain variations.

Low-resolution displacement estimates were obtained by global companding (step 1 in Fig. 2), where the SAD kernels were 20 waveforms $\times$ 200 samples (about 4 mm $\times$ 3 mm), and the size of the search region varied depending on the amount of strain applied. Sixteen nonoverlapping SAD kernels were selected from each precompression echo field in a uniformly-spaced 4×4 grid extending over the entire echo field. The 16 measured displacement vectors were combined in a regression analysis to estimate four parameters: the overall shift and average strain along the y axis and z axis. The precompression echo field was deformed accordingly using nearest-neighbor interpolation between waveforms (y axis) and samples (z axis).

Mid-resolution displacement estimates were obtained by local companding (step 2 in Fig. 2), where the SAD kernel was 6 waveforms $\times$ 60 samples (about 1 mm $\times$ 1.2 mm).

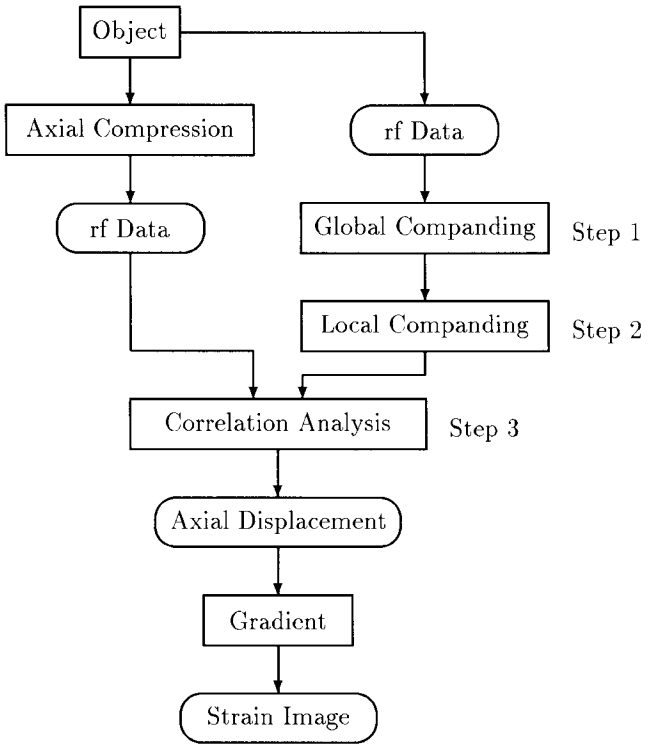

Fig. 2. Flow chart of the experiment and image formation algorithm.

This kernel size balanced the need for low noise and high spatial resolution for displacement given the improved correlation between the pre- and postcompression echo fields following global companding. The SAD kernels of the local compander were highly overlapped. Each data point in the precompression echo field was shifted according to the displacement vector found from the SAD algorithm. Nearest-neighbor interpolation was again used.

High-resolution displacement estimates were obtained between the postcompression and the companded, precompression echo fields by 1-D cross-correlation along the axis of the sound beam (step 3 in Fig. 2). Because the residual strain was very low, typically <0.1%, relatively long data windows, approximately 4 mm (256 points), were used to estimate the point-by-point displacements with high precision to minimize local strain noise. Quadratic interpolation was used to estimate subsample displacements. The shift between correlation windows ΔZ was small, ~0.4 mm, to maximize spatial sampling. The issue of spatial resolution was not investigated in this paper. Strain was estimated from the difference between adjacent displacement pairs ΔD divided by the shift between correlation windows ΔZ, i.e.:

$$\hat{s} = \frac{\Delta D}{\Delta Z}. \tag{1}$$

D. Performance Measures

Three measures of image quality were compared to evaluate the merits of companding in the following studies. Each measure was formed from the regional mean $\overline{\hat{s}}$ and variance $\mathrm{var}(\hat{s})$ of strain estimates. The first measure is image contrast C_I:

$$C_I = \frac{\overline{\hat{s}}_b - \overline{\hat{s}}_t}{\overline{\hat{s}}_b}. \tag{2}$$

$\overline{\hat{s}}_t$ is the average strain for the three target regions and $\overline{\hat{s}}_b$ is the average strain for the background in a region that extends in a strip across the upper half of the image between the top two targets [between lines A and B in Fig. 1(c)]. This region included some object variance in addition to image variance. The second measure is image noise N_I normalized by the average background strain:

$$N_I = \frac{\sqrt{\frac{1}{2}\left(\mathrm{var}(\hat{s})_b + \mathrm{var}(\hat{s})_t\right)}}{\overline{\hat{s}}_b}. \tag{3}$$

Variances were measured in the regions of the respective means.

The third measure is the contrast-to-noise ratio CNR_I,

$$\mathrm{CNR}_I = \frac{C_I}{N_I} = \sqrt{\frac{2(\overline{\hat{s}}_b - \overline{\hat{s}}_t)^2}{\mathrm{var}(\hat{s})_b + \mathrm{var}(\hat{s})_t}}. \tag{4}$$

CNR_I is not a rigorous measure of target detectability. It does not take into account the effects of stress concentration, where the ensemble statistics $E\{\hat{s}\}$ and $E\{(s-\hat{s})^2\}$ are not equal to the regional statistics $\overline{\hat{s}}$ and $\mathrm{var}(\hat{s})$. Also, (4) does not explicitly describe target visibility at different spatial frequencies. However, it does provide a scale for comparing techniques based on large-target contrast and relatively uniform noise that is well correlated with visual impressions and, therefore, is of interest in our study.

III. Results

Three series of phantom experiments were performed. Limitations on maximum applied compression for which 2-D companding restores correlation between pre- and postcompression echo fields were investigated in the first two series. The third series of experiments was performed to investigate the effectiveness of companding for an object under tension.

In the first series, the phantom was constrained to prevent motion on two opposing surfaces along the x axis and scanned in the central y, z plane at $x = 0$. Strain images were formed for applied strains up to about 10% as shown in Fig. 3. With 2-D local companding, image contrast (Fig. 4) increased at a greater rate than noise (Fig. 5) up to 4.8% applied strain where CNR_I was maximum (Fig. 6).

To save time during strain estimation, we have chosen not to include the global companding parameters that give the average longitudinal strain $\overline{\hat{s}}$. Consequently, the value of any pixel i, j indicates $\hat{s}_{i,j} - \overline{\hat{s}}$, and pixel values are either positive or negative such that the average pixel value in each image is zero. Subtracting a constant from an image

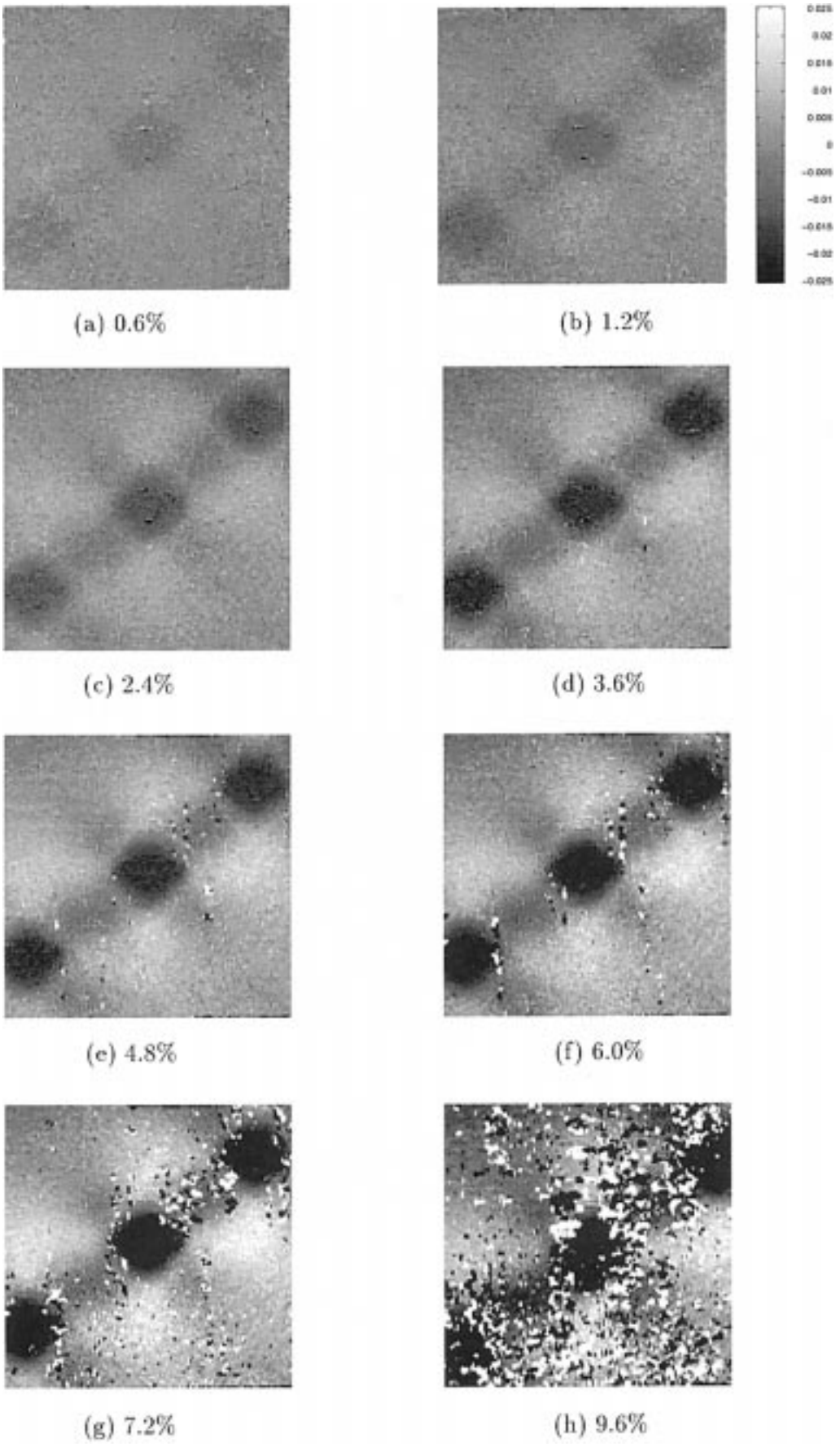

Fig. 3. Longitudinal strain images of the phantom depicted in Fig. 1 using the image formation algorithm of Fig. 2 at several applied strains. Dark regions indicate areas of low strain.

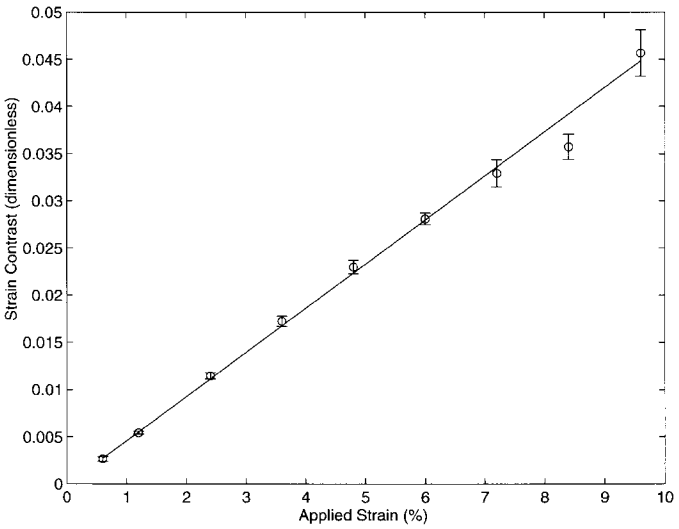

Fig. 4. Target contrast (2) at nine different levels of applied strain. The straight line represents the best linear fit to the data, and the error bars show ± 1 standard deviation. The slope is 0.005.

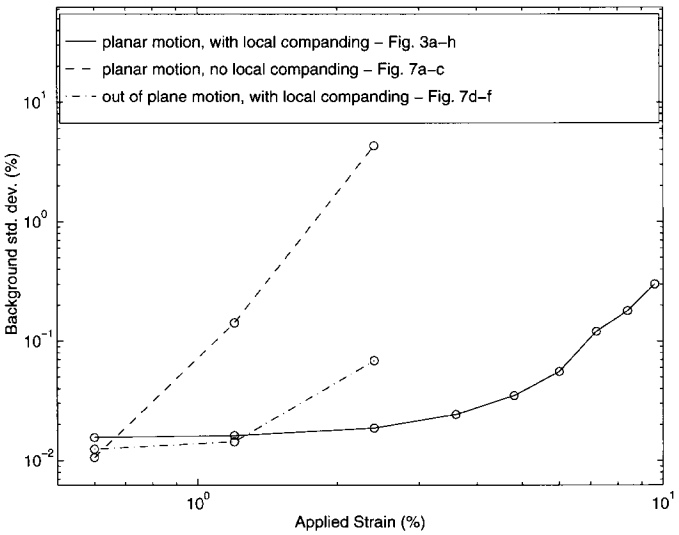

Fig. 5. Standard deviation of strain for the background region as a function of applied strain. Values were obtained using the horizontal section of image data between points A and B, as indicated in Fig. 1(c), and include object variability. The initial slope of the solid line is 13.25×10^{-4}.

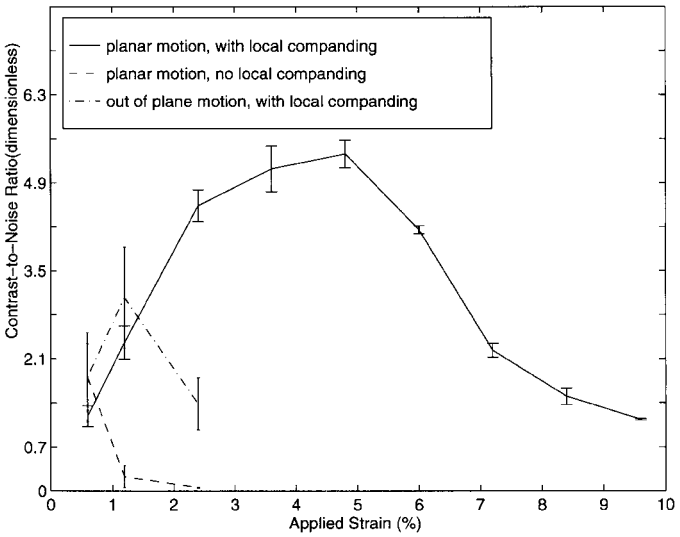

Fig. 6. The contrast-to-noise ratio (CNR_I) (4) is shown for different levels of applied strain.

only affects overall brightness. Nevertheless, image contrast increases in proportion to the applied compression, as seen in Figs. 3 and 4, because the deviation from the average strain increases. The gray-scale display parameters, including brightness, were fixed for all images in this report.

Strain images of the phantom without 2-D local companding are shown in Figs. 7(a)–(c) for applied strains up to 2.4%. Only 1-D global companding along the ultrasound beam was applied to condition signals in Figs. 7(a)–(c). Without 2-D local companding, the uncompensated lateral motion in images with a 40-mm wide field of view produced significant decorrelation even for strains less than 1%. Comparisons with Figs. 3(a)–(c) show 2-D local companding was able to remove all lateral decorrelation noise for this geometry, thus producing a uniform noise pattern that enables inclusion at any location in the field to be equally visible.

In the second series of experiments, the bottom surface of the phantom was fixed to the base plate (bound in x, y, z) by removing the lubrication while the top surface was allowed to freely slip along the compressor face in the x, y plane. Consequently, the top of the phantom provided a region in which elevational motion was present, and the bottom provided a region in which elevational motion was negligible. The linear array was positioned away from the central plane at $x = 25$ mm such that the phantom could move perpendicular to the scan plane of the transducer. The effects of out-of-plane motion on companded signals can be seen by comparing Figs. 7(d)–(f) with Figs. 3(a)–(c), respectively. The decorrelation noise was greatest near the top of the image, where for 2.4% applied strain the out-of-plane displacement was approximately 1/4 (elevational motion for free-slip) × 1/2 (echo field half way to the edge) × 60 mm (distance from the bottom of the phantom to the top of the echo field) × 0.024 (compression) = 0.18 mm. The bound state of the bottom surface appears in the images as a dark region of lower strain.

In the third series of experiments, images of transverse strain were formed by compressing the phantom in a direction perpendicular to the scan axis, as shown in Fig. 8. For these linear, isotropic, incompressible phantom materials, the transverse strain was equal but of opposite sign to the longitudinal strain when the motion is confined to the scan plane. There was no motion along the x axis, so the maximum displacement along y was half that along z. We inverted the sign of the transverse strain estimates for the comparison in Fig. 8. The two images are very similar, which is consistent with our assumption that the gelatin phantoms are incompressible and the strain tensor com-

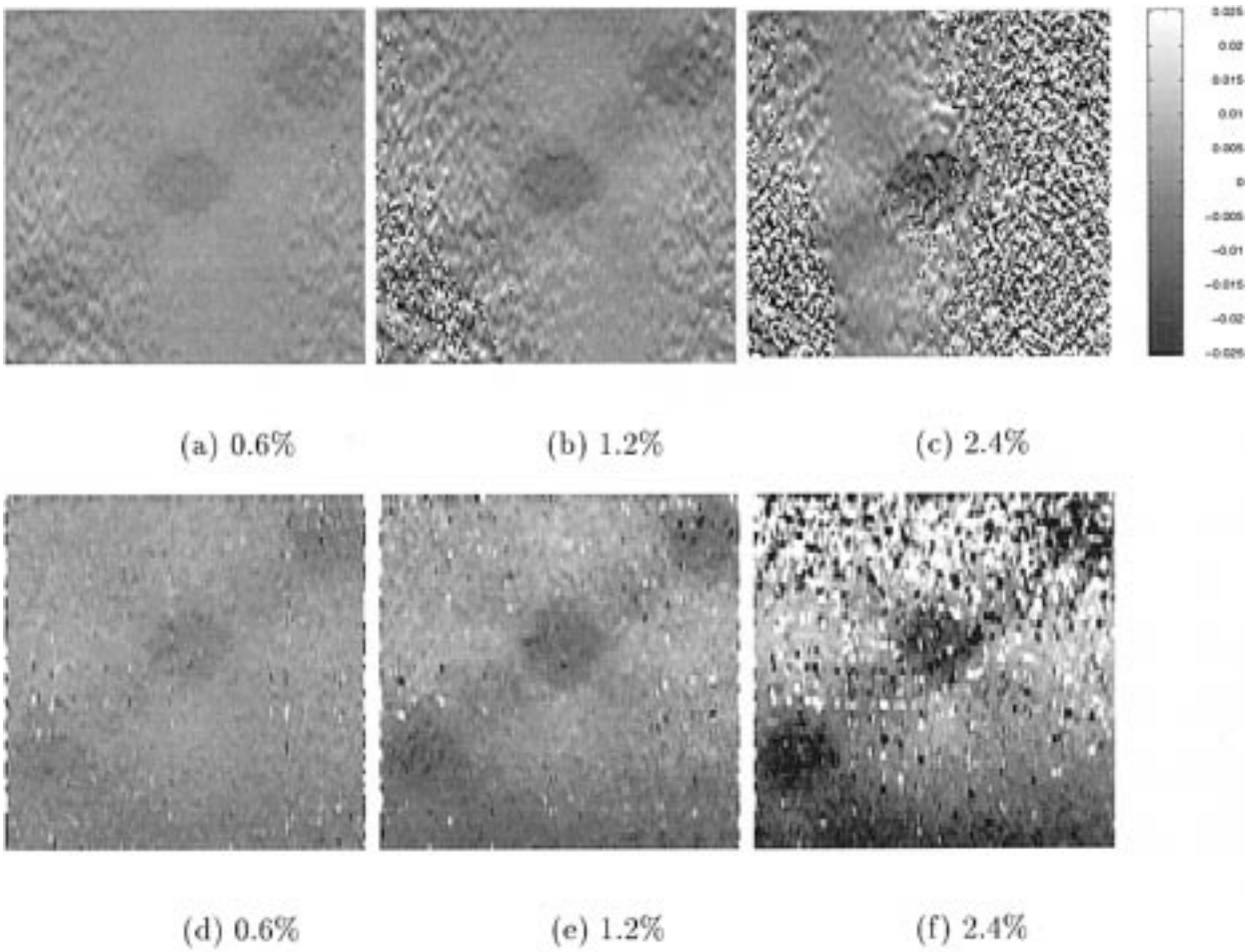

Fig. 7. Longitudinal strain images of the phantom depicted in Fig. 1 for different boundary conditions and different types of processing: (a)–(c) are with no elevational motion when processed without local companding, (d)–(f) include the effects of out-of-plane motion with 2-D local companding.

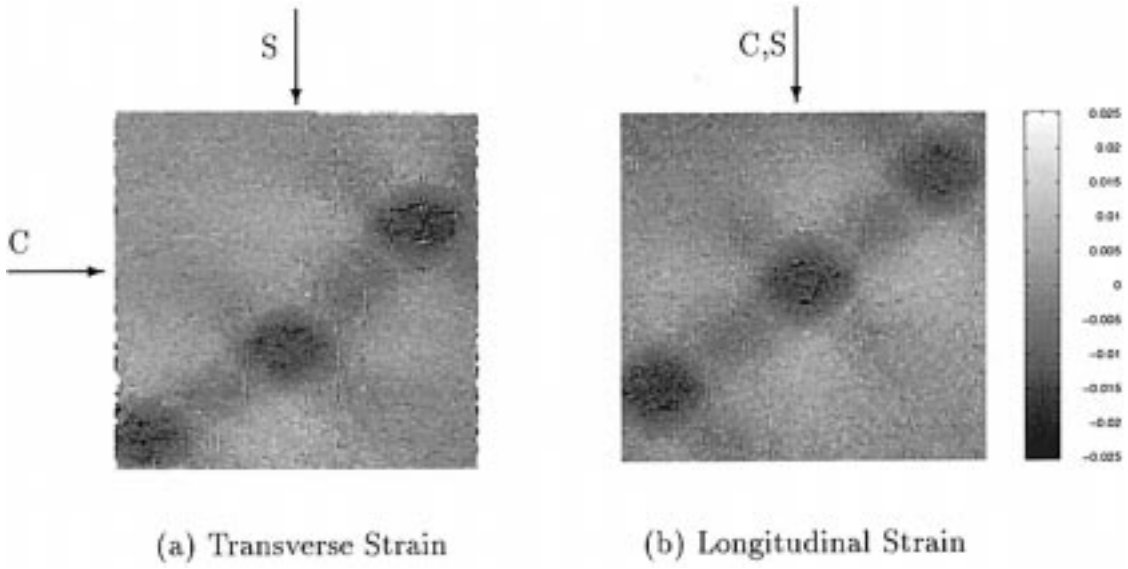

Fig. 8. Transverse and longitudinal strain images of the phantom depicted in Fig. 1 for 2.4% applied strain. Companding was used and motion was confined to the scan plane. C indicates the direction of compression; S indicates the direction of transmitted ultrasound pulses.

ponents s_{zz} and s_{zy} are equal and opposite.

Companding improves image quality at the expense of computation time. Typically, the 2-D local companding (step 2 in Fig. 2) increases the total time required to form a strain image from 2 to 20 min on a workstation running a combination of FORTRAN and Matlab programs that have not been optimized for speed. Parallel processing techniques could reduce the image formation time significantly.

IV. Discussion

Nonaxial object motion encompasses translations normal to the beam axis in (lateral) or out (elevational) of the scan plane, rotation, and shear. The images of Fig. 3 indicate that, if the object motion is confined to a scan plane that is finely sampled and rotation and shear motions are minimal, then 2-D companding produces strain images with noise that does not increase with applied strain up to about 5% (Fig. 5). Constant noise implies that strain estimates are limited by the SNR of the ultrasound signals. The increase in noise at larger applied strains results from instantaneous signal decorrelation or rotational and shear motion that these block-matching algorithms cannot detect.

Regarding sampling, the 5 MHz, f/2 (in-plane) linear array with multiple transmit focal zones and dynamic focus on receive had a lateral beam width of approximately 1.2 mm. At the echo line density of 5 mm^{-1}, there were approximately three A-lines per half lateral beam width, which proved sufficient for removing lateral decorrelation effects up to 10% strain. A lower lateral sampling rate may be insufficient for accurately tracking object motion at such high applied strains.

For applied strains greater than 5%, companding was unable to fully restore signal decorrelation, particularly near stiff inclusions. Fig. 6 indicates that the increase in noise surpassed the increase in contrast for applied strains greater than 5%. The images of Fig. 3 show that companding also leads to spatially uniform noise properties up to 5% applied strain. Current breast elastography that uses 1-D global companding is limited to 1% applied strain [1], [2] to minimize the decorrelation noise seen in Figs. 7(a)–(c). This phantom study suggests that companding has the potential for increasing CNR_I fivefold for breast imaging by providing greater contrast with higher applied strains without suffering from significant decorrelation noise. The higher level of applied strain possible with local companding translates directly into higher contrast (Fig. 4) and improved target visibility (Fig. 6) while avoiding the disadvantages of multicompression techniques. A combination of multicompression and companding may be of interest in situations where applied strains greater than 5% are needed.

Another noticeable feature of the companded images of Fig. 3 is that noise within the inclusions is lower than noise in the background. For example, at 2.4% compression [Fig. 3(c)] the standard deviation is 0.04 in the background and 0.03 inside the inclusions. The background is soft and deformable, but these inclusions are relatively hard. Therefore, each target translates as a rigid body with little strain when suspended in the softer medium. Axial translation without strain preserves signal correlation, even without companding [6]. However, 2-D local companding is necessary to correct for lateral motion, as observed in Figs. 3 and 7.

The 2-D local companding was much less effective for geometries that permitted large elevational motion. There can be no data kernel (SAD kernel for our technique) in the postcompression echo field that matches one in the precompression echo field when scatterers move out of the plane. Similarly, the block matching algorithm does not test for object rotation or shear. The companding algorithm produced large displacement errors in the presence of out-of-plane motion that were compounded by the subsequent cross-correlator, so the strain noise was relatively high for 2.4% applied strain (Fig. 5) and target visibility was low (Fig. 6). Furthermore, unlike the decorrelation noise caused by lateral motion, the noise caused by elevational motion was uniform across the upper half of the image where the object was allowed to move [Fig. 7(d)–(f)]. The noise patterns are a function of the boundary conditions of the phantom.

Figs. 5 and 6 illustrate additional merits and limitations of 2-D local companding. Companding provides another weak source of noise in the strain image due to the variance of the displacement estimate at the local companding stage. When the applied strain was less than 1%, decorrelation errors were negligible so that the small amount of noise introduced by local companding increased the overall image noise. Although, compared to the geometry that permitted out-of-plane motion, the noise was slightly lower and the CNR_I higher for small compressions when local companding was used and object motion was in the scan plane, the relatively large errors in our estimates (Fig. 6) indicate that the differences are statistically insignificant. Target detectability was improved with 2-D local companding for applied strains between 1 and 7% when the object motion was confined to the scan plane. Noise reduction exceeded two orders of magnitude at 2.4% strain (Fig. 5) by minimizing the effects of time-averaged signal decorrelation.

Fig. 6 showed that between 2 and 6% applied strain, the CNR_I was nearly constant when 2-D local companding was used. The increase in contrast, Fig. 4, was offset by an increase in noise, Fig. 5. The peak in the CNR_I versus strain curve in Fig. 6 depends on several experimental parameters including the size of the SAD kernel, length of the correlation window, dimensions of each pixel in the strain image (window overlap), and the relative stiffness of the inclusions and the background materials. The phantom background and target stiffnesses were selected to mimic the average elastic properties of normal breast parenchyma and cancerous tissues at 5% precompression, respectively [16]. The length and overlap of the correlation windows were selected to obtain a visually "optimal" combination of noise and detail. However, a study was

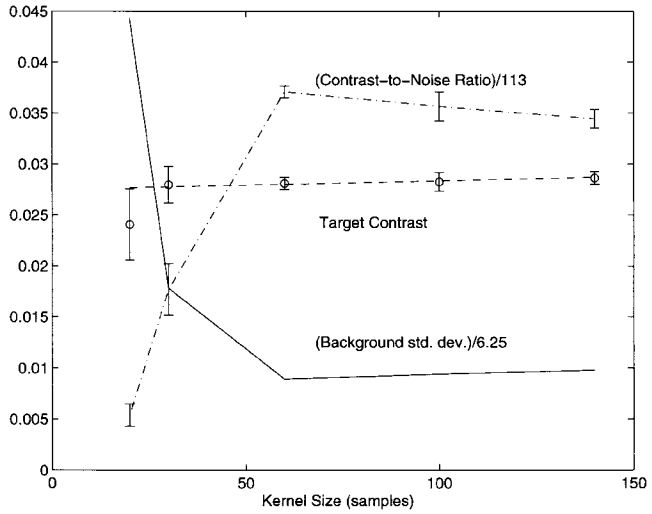

Fig. 9. Target contrast (dimensionless), background standard deviation (%), and contrast-to-noise ratio (dimensionless) for 6% applied strain as a function of the SAD kernel size used for local companding. The horizontal axis shows the axial dimension of the kernel; the lateral dimension was adjusted to maintain a square kernel.

conducted to understand the effects of SAD kernel size on N_I and CNR_I for 6% applied strain as summarized in Fig. 9. While the contrast away from material boundaries is approximately constant over the range of kernel sizes investigated, the background noise decreases rapidly up to 60 samples (1.2 mm), where CNR_I reaches its maximum value. Larger kernel sizes increase displacement estimation errors when strain is present [6].

V. Conclusions

Compared to 1-D global companding, 2-D local companding improved target detectability in strain images by minimizing decorrelation noise and allowing higher applied strains that increased image contrast. Large-target visibility, as measured by CNR_I, was improved for applied strains between 1 and 7% and was maximum at 5% when 2-D local companding was used. At higher strains, local companding was unable to restore correlation between pre- and postcompression echo fields. 2-D local companding significantly increased the dynamic range for strain imaging as compared to the 1-D global companding methods now in use (Fig. 6). Also, the noise patterns are spatially uniform over a 40 mm × 40 mm field of view. The 2-D local companding virtually eliminated noise in strain images due to lateral motion and time-averaged signal decorrelation in the absence of elevational motion, but was less effective when out-of-plane motion was present. Consequently, it is important to confine object motion to the scan plane to realize the full benefits of 2-D local companding.

References

[1] I. Céspedes, J. Ophir, H. Ponnekanti, and N. Maklad, "Elastography: Elasticity imaging using ultrasound with application to muscle and breast in vivo," *Ultrason. Imaging*, vol. 15, pp. 73–88, 1993.

[2] B. S. Garra, E. I. Céspedes, J. Ophir, S. R. Spratt, R. A. Zuurbier, C. M. Magnant, and M. F. Pennanen, "Elastography of breast lesions: Initial clinical results," *Radiology*, vol. 202, pp. 79–86, 1997.

[3] S. Y. Emelianov, M. A. Lubinski, W. F. Weitzel, R. C. Wiggins, A. R. Skovoroda, and M. O'Donnell, "Elasticity imaging for early detection of renal pathology," *Ultrason. Med. Biol.*, vol. 21, pp. 871–883, 1995.

[4] M. O'Donnell, A. R. Skovoroda, B. M. Shapo, and S. Y. Emelianov, "Internal displacement and strain imaging using ultrasonic speckle tracking," *IEEE Trans. Ultrason., Ferroelect., Freq. Contr.*, vol. 41, pp. 314–325, 1994.

[5] J. Ophir, I. Céspedes, H. Ponnekanti, Y. Yazdi, and X. Li, "Elastography: A quantitative method for imaging the elasticity of biological tissues," *Ultrason. Imaging*, vol. 13, pp. 111–134, 1991.

[6] M. Bilgen and M. F. Insana, "Error analysis in acoustic elastography: I. Displacement estimation; II. Strain estimation and SNR analysis," *J. Acoust. Soc. Amer.*, vol. 101, pp. 1139–1146 and 1147–1154, 1997.

[7] J. W. Betz, "Effects of uncompensated relative time companding on a broad-band cross correlator," *IEEE Trans. Acoust., Speech, Signal Processing*, vol. ASSP-33, pp. 505–510, 1985.

[8] P. Chaturvedi, M. F. Insana, and T. J. Hall, "2-D companding for noise reduction in strain imaging," *IEEE Trans. Ultrason., Ferroelect., Freq. Contr.*, vol. 45, pp. 179–191, Jan. 1998.

[9] D. I. Barnea and H. F. Silverman, "A class of algorithms for fast digital image registration," *IEEE Trans. Comput.*, vol. C-21, pp. 179–186, 1972.

[10] Ross, H. L. Schaffer, A. Cohen, R. Freudberg, and H. J. Manley, "Average magnitude difference function pitch extractor," *IEEE Trans. Acoust., Speech, Signal Processing*, vol. ASSP-22, pp. 353–362, 1974.

[11] L. N. Bohs and G. E. Trahey, "A novel method for angle independent ultrasonic imaging of blood flow and tissue motion," *IEEE Trans. Biomed. Eng.*, vol. 38, pp. 280–286, 1991.

[12] I. Céspedes and J. Ophir, "Reduction of image noise in elastography," *Ultrason. Imaging*, vol. 15, pp. 89–102, 1993.

[13] C. H. Knapp and G. C. Carter, "Estimation of time delay in the presence of source or receiver motion," *J. Acoust. Soc. Amer.*, vol. 61, pp. 1545–1549, 1977.

[14] J. Meunier, M. Bertrand, and G. Mailloux, "A model for dynamic texture analysis in two-dimensional echocardiograms of the myocardium," *Proc. SPIE*, vol. 786, pp. 193–200, 1987.

[15] T. Varghese, J. Ophir, and I. Céspedes, "Noise reduction in elastograms using temporal stretching with multicompression averaging," *Ultrason. Med. Biol.*, vol. 22, pp. 1043–1052, 1996.

[16] T. J. Hall, M. Bilgen, M. F. Insana, and T. A. Krouskop, "Phantom materials for elastography," *IEEE Trans. Ultrason., Ferroelect., Freq. Contr.*, vol. 44, pp. 1355–1365, 1997.

[17] T. J. Hall, M. F. Insana, L. A. Harrison, and G. G. Cox, "Ultrasonic measurement of glomerular diameters in normal adults," *Ultrason. Med. Biol.*, vol. 22, pp. 987–997, 1996.

Pawan Chaturvedi (S'91–M'92–S'93–M'95) was born in Katni, India on January 21, 1968. He received the B.Sc. (Honors) degree in physics from the University of Delhi in 1988, M.Sc. in physics from the Indian Institute of Technology, Delhi in 1990, M.S. in electrical engineering from Tulane University, New Orleans in 1992, and a Ph.D. in electrical engineering from the University of Kansas in 1995. During the summer of 1989, he was a visiting researcher at the Tata Institute of Fundamental Research, Bombay. From 1990 to 1995 he held teaching and research assistant positions at Tulane University and the University of Kansas. Since 1995, he has been with the Department of Radiology at the University of Kansas Medical Center in Kansas City, where he is currently an Assistant Professor. His research interests are primarily in the fields of inverse problems, acoustic and electromagnetic imaging, and signal and image processing.

He is a member of IEEE, Tau Beta Pi, Eta Kappa Nu and Phi Beta Delta.

Michael F. Insana (M'85) was born in Portsmouth, VA on December 18, 1954. He received the B.S. degree in physics from Oakland University, Rochester, MI in 1978 and the M.S. and Ph.D. degrees in medical physics from the University of Wisconsin, Madison, WI in 1982 and 1983, respectively. From 1984 to 1987 he was a research physicist at the FDA's Center for Devices and Radiological Health, where he worked in medical imaging with emphasis on acoustic signal processing. He is currently Associate Professor of Radiology at the University of Kansas Medical Center. His current research interests are acoustic imaging and tissue characterization, signal detection and estimation, observer performance measurements, and image quality assessment. He is a member of the IEEE, SPIE, ASA, AIUM, and AAPM professional societies.

Timothy J. Hall (M'88) received a B.A. in physics from the University of Michigan-Flint in 1983, and M.S. and Ph.D. in Medical Physics from the University of Wisconsin-Madison in 1985 and 1988, respectively.

He is currently an Associate Professor in the Department of Radiology at The University of Kansas Medical Center. Dr. Hall's research interests include quantitative ultrasonic and elastographic imaging, and measures of observer performance and image quality.

Dr. Hall is a member of the IEEE, the Acoustical Society of America, and the American Association of Physicists in Medicine.